ACS APPLIED MATERIALS & INTERFACES

Research Article

www.acsami.org

Multifunctional Theranostics for Dual-Modal Photodynamic Synergistic Therapy via Stepwise Water Splitting

Dan Yang,[†] Guixin Yang,[†] Shili Gai,[*,†] Fei He,[†] Chunxia Li,[‡] and Piaoping Yang[*,†]

[†]Key Laboratory of Superlight Materials and Surface Technology, Ministry of Education, College of Material Sciences and Chemical Engineering, Harbin Engineering University, Harbin 150001, P. R. China

[‡]College of Chemistry and Life Sciences, Zhejiang Normal University, Jinhua 321004, P. R. China

Supporting Information

ABSTRACT: Combined therapy using multiple approaches has been demonstrated to be a promising route for cancer therapy. To achieve enhanced antiproliferation efficacy under hypoxic condition, here we report a novel hybrid system by integrating dual-model photodynamic therapies (dual-PDT) in one system. First, we attached core−shell structured up-conversion nanoparticles (UCNPs, $NaGdF_4$:Yb,Tm@$NaGdF_4$) on graphitic-phase carbon nitride (g-C_3N_4) nanosheets (one photosensitizer). Then, the as-fabricated nanocomposite and carbon dots (another photosensitizer) were assembled in ZIF-8 metal−organic frameworks through an in situ growth process, realizing the dual-photosensitizer hybrid system employed for PDT via stepwise water splitting. In this system, the UCNPs can convert deep-penetration and low-energy near-infrared light to higher-energy ultraviolet−visible emission, which matches well with the absorption range of the photosensitizers for reactive oxygen species (ROS) generation without sacrificing its efficacy under ZIF-8 shell protection. Furthermore, the UV light emitted from UCNPs allows successive activation of g-C_3N_4 and carbon dots, and the visible light from carbon dots upon UV light excitation once again activate g-C_3N_4 to produce ROS, which keeps the principle of energy conservation thus achieving maximized use of the light. This dual-PDT system exhibits excellent antitumor efficiency superior to any single modality, verified vividly by in vitro and in vivo assay.

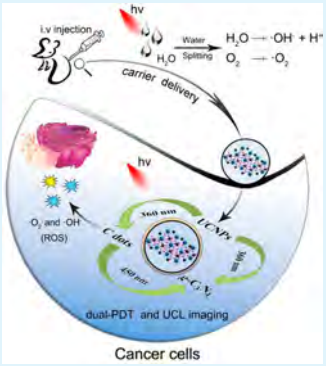

KEYWORDS: *up-conversion, g-C_3N_4, carbon dots, MOFs, synergistic therapy*

INTRODUCTION

Nowadays, dual-model photodynamic therapies (dual-PDT), combining two kinds of photosensitizers as potential collaborators in one system, may pave the avenue toward the clinical application of photodynamic treatment, because all photosensitizers are flawed.[1−5] It is well-known that the three elements of PDT in the treatment process are the excited laser, photosensitizer, and oxygen in tissue. In the presence of light excitation, photosensitizers can transfer the absorbed photon energy to surrounding oxygen molecules, generating reactive oxygen species (ROS) including free radicals ($\cdot O_2^-$) or singlet oxygen ($^1O_2$) and consequently introduce cancer cell death and tissue damage theoretically.[6−12] Therefore, hypoxia is one of the formidable adversaries to high-efficiency photodynamic treatment, because PDT-induced oxygen consumption is an irreversible process.[13−16] Normoxic region in the outermost layers of the tumor can guarantee oxygen concentration to PDT, but the absence of oxygen restricts the efficiency of photosensitizers in the hypoxic and necrotic areas of solid tumors ($pO_2 \leq 2.5$ mmHg).[17−20] Furthermore, because most photosensitizers are activated by ultraviolet light or visible light, in vivo tumor growth inhibition efficacy of PDT has been restricted by the low tissue penetration depth of ultraviolet light or visible light, which cannot pass through thick tissue.[21−25] Therefore, the appropriate combination of dual-model PDT, which can be mediated by high-penetration near-infrared (NIR) light, should be capable of solving the above problem.

Recently, Kang and co-workers reported efficient photocatalyst for stable visible water splitting by attaching carbon dots (CDs) on g-C_3N_4 sheets.[26] Notably, compared with absorption peak of g-C_3N_4, the absorption intensity over the entire wavelength range has been greatly increased after incorporating CDs on the g-C_3N_4 matrix. The research on this point inspires us that the combination of g-C_3N_4 and CDs may constitute a high-performance photosensitizer for PDT via the stepwise water splitting: (i) $2H_2O \rightarrow H_2O_2 + H_2$; (ii) $2H_2O_2 \rightarrow 2H_2O + O_2$.[27,28] Meanwhile, g-C_3N_4 is an earth-abundant and low-cost photocatalyst capable of generating H_2 and H_2O_2 from water even in the absence of catalytic metals and can be easily prepared.[29−33] In addition, as photosensitizer, g-C_3N_4 nanosheets are able to generate ROS and kill cancer cells efficiently under very low-intensity light irradiation (20 mW/cm^2).[6,34−37] Moreover, as a new class of monodisperse carbon materials below 10 nm in diameter, CDs exhibit unique photoinduced electron transfer, electron reservoir properties, and photoluminescence properties.[38−42] Taking advantage of remarkable excitation wavelength-dependent photolumines-

Received: November 27, 2016
Accepted: February 7, 2017
Published: February 7, 2017

DOI: 10.1021/acsami.6b15203
ACS Appl. Mater. Interfaces 2017, 9, 6829−6838

Scheme 1. Schematic Illustration of the Formation Process of UCNPs-*g*-C_3N_4−CDs@ZIF-8 Composite

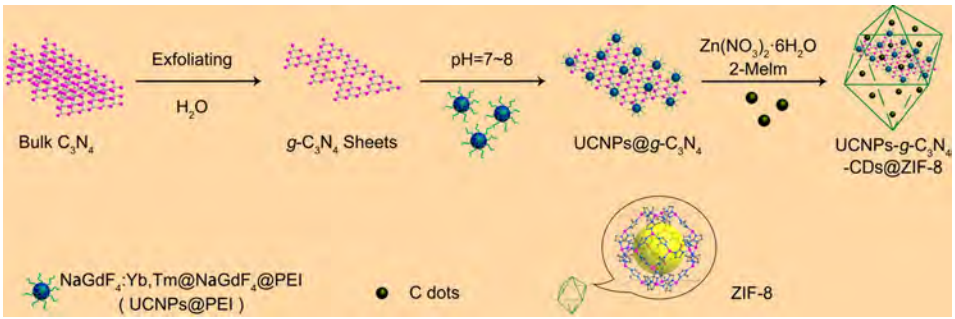

cence property, high photostability, good water solubility, easy surface functionalization, good biocompatibility, and low toxicity, CDs have been applied as nanocarriers for the delivery of photosensitizers, chemotherapy drugs, and therapeutic gene agents.[43−47] Interestingly, researchers found that the CDs have any analogous peroxidase behavior, which possess high catalytic activity for H_2O_2 decomposition to produce oxygen even no light is required.[39,48−50]

Even if the combination of *g*-C_3N_4 and CDs may preliminarily solve low tissue penetration depth of UV−vis light to activate single conventional photosensitizer, whether the PDT efficacy of *g*-C_3N_4−CDs composite excited by NIR laser is higher than those of CDs and *g*-C_3N_4 excited by UV−vis light has never been ascertained. This is because the UV−vis light absorption intensity is considerably stronger than the NIR light absorption intensity of *g*-C_3N_4 even with a masterstroke of CDs. Fortunately, the up-conversion nanoparticles (UCNPs) can transfer deeply penetrating low-energy NIR light to higher-energy UV−vis light, which matches the activation absorption spectra of photosensitizers. Integration of UCNPs with dual photosensitizers can efficiently generate ROS at deep depth without sacrificing its efficacy, which is capable of solving the above problems, when the composite is protected by the metal−organic frameworks (MOFs) shell.[51−59] In the UCNPs-*g*-C_3N_4−CDs composite, the UV−vis light emitted from UCNPs upon 980 nm laser excitation allows successive activation of *g*-C_3N_4 and CDs, and the excited visible light from CDs can once again activate *g*-C_3N_4 for ROS production, which achieve the maximized use of the energy.

Selecting the highly water-soluble MOFs as the shell can ensure the stability of dual-PDT system and store abundant oxygen and water for PDT use. Especially, the ZIF-8 MOFs have some interesting characteristics including large specific surface area, ordered pores with tunable size and volume, progressive biodegradability, and low cytotoxicity.[60−63] There have been two special advantages for MOFs to be concerned, namely, the excellent hydrophilic property, which can store abundant water for PDT, and good capping effect, which can prevent the fluorescence intensity of encapsulated UCNPs from being affected by the surroundings, which is much different from and superior to mesoporous silica.[64−66]

In this study, we fabricated a dual-model photodynamic synergistic therapy platform based on MOFs of UCNPs-*g*-C_3N_4−CDs@ZIF-8 particles fabricated by an in situ growth process, realizing the dual-PDT hybrid system employed for PDT via stepwise water splitting. The inhibition effect of tumor proliferation is surveyed on cervical cancer cells both in vitro and in vivo. The survey results may provide important implications for UCNPs-*g*-C_3N_4−CDs@ZIF-8 application in the future treatment of cancer and provide an avenue for developing drug nanocarriers with enhanced photodynamic therapeutic efficiency for promising clinical applications.

RESULTS AND DISCUSSION

The formation process of UCNPs-*g*-C_3N_4−CDs@ZIF-8 dual-PDT theranostic platform is schematically illustrated in Scheme 1. Briefly, ultrathin *g*-C_3N_4 nanosheets were prepared by heat polymerization of melamine couple with liquid exfoliation of bulk C_3N_4, and a simple electrostatic attraction participates in the process of subsequent UCNPs-*g*-C_3N_4. Finally, the resulting theranostic platform, UCNPs-*g*-C_3N_4−CDs@ZIF-8, is synthesized by an encapsulation of UCNPs-*g*-C_3N_4 and CDs into the metal−organic frameworks (ZIF-8) in an in situ process. Oleic acid (OA)-stabilized $NaGdF_4$:Yb,Tm@$NaGdF_4$ nanoparticles were first synthesized through thermal decomposition of corresponding rare earth oleates. Poly(ethylenimine) (PEI)-coated UCNPs (UCNPs-PEI) were then synthesized by a facile ligand exchange method to convert hydrophobic OA-capped UCNPs into hydrophilic ones. PEI polymer with charged surface capped on the UCNPs also plays an important role in the interaction with charged *g*-C_3N_4 nanosheets at the approximate neutral environment, whose mechanism is generally known as proton sponge effect.[67] The successful modification of PEI on UCNPs can be partially proved by Fourier transform infrared spectroscopy (FT-IR) spectra (Figure S1). The characteristic peaks at ∼3434 cm^{-1} (ν_{N-H}) and 1563 cm^{-1} (δ_{N-H}) are indicative of the stretch vibration and deformation vibrations of the N−H bond in the $-NH_2$ group.

In Figure 1A−D, $NaGdF_4$:Yb,Tm and $NaGdF_4$:Yb,Tm@$NaGdF_4$ consist of monodisperse nanoparticles with an average diameter of ∼11 and 16 nm, respectively. The transmission electron microscopy (TEM) image of *g*-C_3N_4 nanosheets demonstrates a two-dimensional sheetlike structure with thickness of less than 5 nm (Figures 1E and S2). The highly disperse and nearly transparent nature of ultrathin *g*-C_3N_4 nanosheets in water is illustrated in inset of Figure 1E. The TEM images of UCNPs-*g*-C_3N_4 composite indicate that UCNPs are well-dispersed on the *g*-C_3N_4 nanosheets (inset in Figure 1F). TEM image of UCNPs-*g*-C_3N_4−CDs@ZIF-8 composite is displayed in Figure 1F,G. As shown, the composite displays a polyhedron structure with diameter of ∼150 nm; thus, it should quickly be engulfed by organs such as liver and spleen, which will help the therapeutic effect. Additionally, no UCNPs-*g*-C_3N_4 particles can be found due to the limited electron penetration depth and the nearly transparent nature of *g*-C_3N_4. Furthermore, the energy-dispersive X-ray analysis (EDXA) pattern (Figure 1H)

DOI: 10.1021/acsami.6b15203
ACS Appl. Mater. Interfaces 2017, 9, 6829−6838

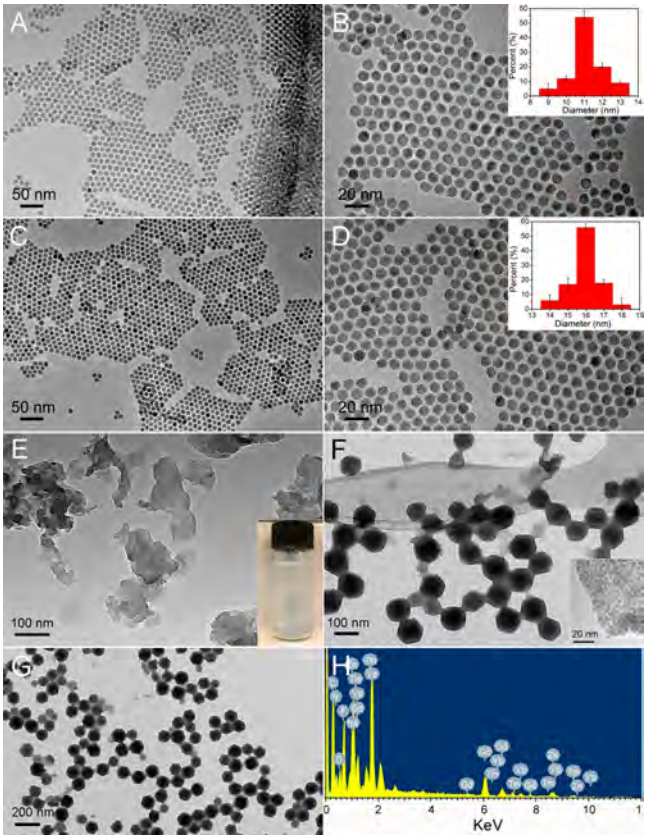

Figure 1. (A) Low- and (B) high-magnified TEM images of $NaGdF_4$:Yb,Tm. (C) Low- and (D) high-magnified TEM images of $NaGdF_4$:Yb,Tm@$NaGdF_4$. (C, D insets) The corresponding particle size distribution. TEM image of (E) g-C_3N_4 nanosheets. TEM image (F, G) and EDS (H) of UCNPs-g-C_3N_4−CDs@ZIF-8. (E, inset) The solution of g-C_3N_4 nanosheets dispersed in water. (F, inset) The TEM image of UCNPs-g-C_3N_4.

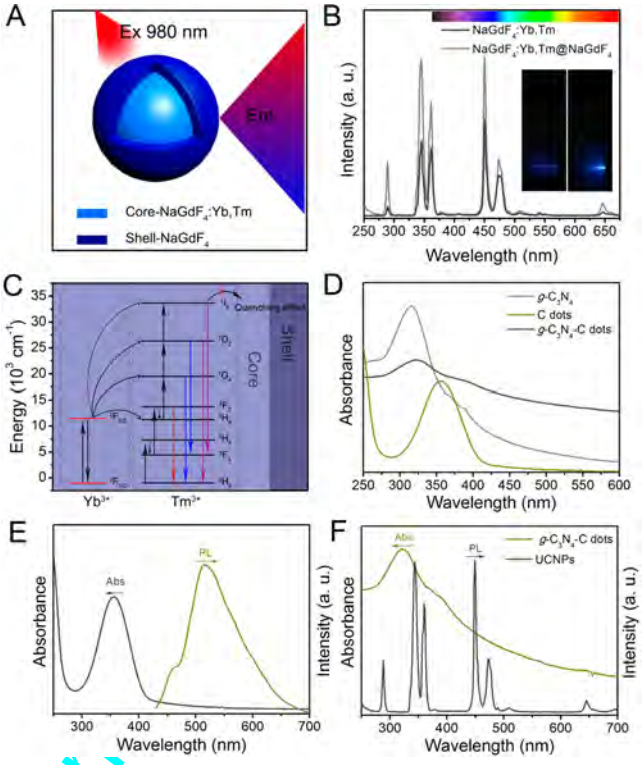

Figure 2. (A) Schematic illustration of the proposed $NaGdF_4$:Yb,Tm@$NaGdF_4$ structure. (B) UC emission spectra of $NaGdF_4$:Yb,Tm and $NaGdF_4$:Yb,Tm@$NaGdF_4$ under 980 nm laser excitation. (insets) Photographs of $NaGdF_4$:Yb,Tm (left) and $NaGdF_4$:Yb,Tm@$NaGdF_4$ (right) particles under 980 nm irradiation. (C) Proposed energy-transfer mechanism of Yb- and Tm-doped nanoparticles upon 980 nm laser excitation. (D) UV−vis absorbance spectra of g-C_3N_4, CDs, and g-C_3N_4−CDs. (E) The emission spectrum upon 360 nm excitation and the absorption spectrum of CDs. (F) The emission spectrum of $NaGdF_4$:Yb,Tm@$NaGdF_4$ under 980 nm laser excitation and the absorption spectrum of g-C_3N_4−CDs photosensitizer.

identifies the presence of Na, Gd, F, Yb, Tm, and Zn elements in the composite. Meanwhile, the powder X-ray diffraction (XRD) pattern of UCNPs-g-C_3N_4−CDs@ZIF-8 composite confirms that the diffraction peaks are assigned to the g-C_3N_4 nanosheets, hexagonal $NaGdF_4$, and ZIF-8 (Figure S3). The results give the evidence for the encapsulation of the UCNPs-g-C_3N_4 and CDs particles in ZIF-8 matrix. The N_2 adsorption/desorption isotherm presents the typical II-type of UCNPs-g-C_3N_4−CDs@ZIF-8, which is characteristic of typical macroporous materials suitable for carrying O_2 or H_2O for PDT. The specific surface area is calculated to be 769 cm^2/g (Figure S4). All above results imply that UCNPs-g-C_3N_4−CDs@ZIF-8 composite may be qualified for the role of anticancer therapeutic platform.

In the schematic illustration of the proposed $NaGdF_4$:Yb,Tm@$NaGdF_4$ structure (Figure 2A), the core−shell structured nanoparticles can emit strong up-conversion (UC) emission under excitation of 980 nm laser. In Figure 2B, the emission spectra contain three distinct Tm^{3+} peaks: a strong and moderate peak at 338 and 360 nm, a strong and moderate peak at 450 and 475 nm, and a weak peak at 645 nm, corresponding to the transitions of Tm^{3+} ions from $^1I_6$ to $^3F_4$ and $^1D_2$ to $^3H_6$, from $^1D_2$ to $^3F_4$ and $^1G_4$ to $^3H_6$, and from $^3F_2$ to $^3H_6$, respectively (Figure 2C).[68] Note that the coating of $NaGdF_4$ layer on $NaGdF_4$:Yb,Tm particles can effectively enhance the emission intensity. In Figure S5, compared with pure UCNPs, the obvious decrease of emission intensity especially in the UV region of UCNPs-g-C_3N_4−CDs@ZIF-8 indicates the effective energy transfer from UCNPs to the two photosensitizers (g-C_3N_4 and CDs), which is capable of activating oxygen molecules to produce ROS.

The UV−vis absorbance spectra of g-C_3N_4, CDs, and g-C_3N_4−CDs indicate the obvious enhancement of visible absorption of g-C_3N_4−CDs after the introduction of CDs (Figure 2D). Meanwhile, as shown in Figure 2E, CDs can emit down-conversion emission under UV light excitation. Accordingly, UCNPs ($NaGdF_4$:Yb,Tm@$NaGdF_4$) convert low-energy NIR light to higher-energy UV−vis light and then transport photon energy to dual photosensitizers to generate ROS due to the overlap of UV−vis emission and absorption of the photosensitizers (Figure 2F). Furthermore, in the g-C_3N_4−CDs composite, the emitted UV−vis light from UCNPs upon NIR light excitation allows successive activation of g-C_3N_4 and CDs, and the visible light (blue) from CDs may once again activate g-C_3N_4 to produce ROS, realizing the maximized use of the energy.

Figure 3A shows the mechanism of the g-C_3N_4 mediated water-splitting process. g-C_3N_4 nanosheets activated by UV−vis light transmit the energy to water, which will induce the splitting reaction of water (theoretical band gap is 1.23 eV) and

DOI: 10.1021/acsami.6b15203
ACS Appl. Mater. Interfaces 2017, 9, 6829−6838

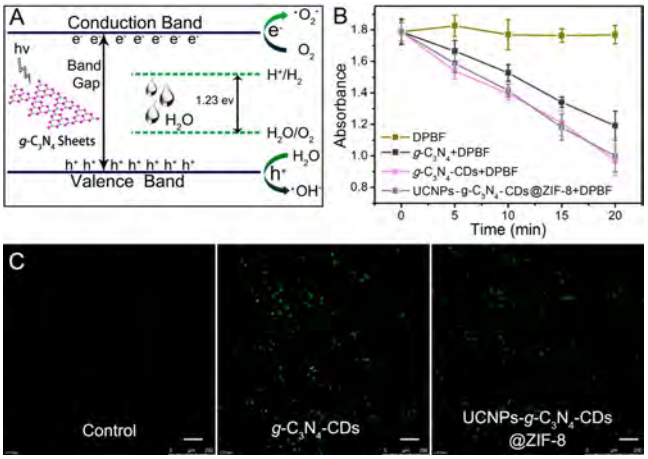

Figure 3. (A) Schematic illustration of the g-C_3N_4 mediated water-splitting process. (B) Decay curves of DPBF absorption at 410 nm in different solutions as a function of the laser irradiation time. (C) CLSM images of HeLa cells incubated with PBS (control), g-C_3N_4−CDs under UV light irradiation, and UCNPs-g-C_3N_4−CDs@ZIF-8 under 980 nm laser irradiation. All the cells were marked with DCFH-DA. Scale bars for all images are 100 μm.

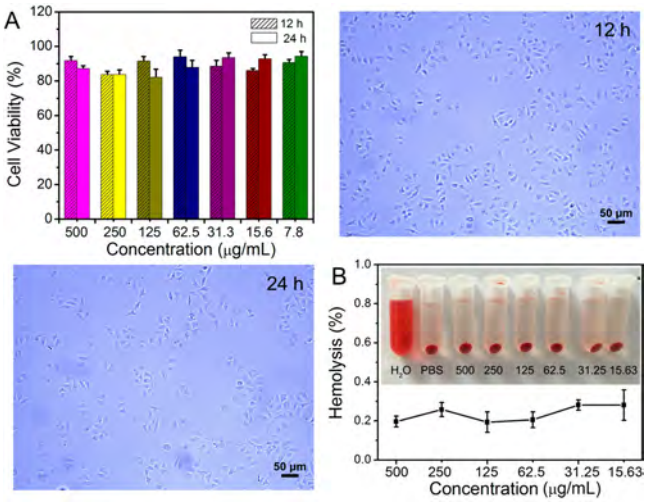

Figure 4. (A) Cell viability for L929 cells incubated with 0.1 mL of UCNPs-g-C_3N_4−CDs@ZIF-8, with different concentrations for 12 and 24 h, and morphology of L929 cells incubated for 12 and 24 h. Scale bars for all images are 50 μm. Cell viability was measured by MTT assay. Data represent mean ± standard deviation (n = 3). (B) Hemolytic assay of UCNPs-g-C_3N_4−CDs@ZIF-8 by human red blood cells.

produce abundant ROS ($\cdot O_2^-$ and $\cdot OH^-$). Then, the ROS sensor agent 1,3-diphenylisobenzofuran (DPBF) is employed to detect the ROS generation ability in dimethyl sulfoxide (DMSO) solution of tested materials. As shown in Figure 3B and Figure S6, compared with only DPBF exposed to NIR laser, the absorption of DPBF solutions containing UCNPs-g-C_3N_4−CDs@ZIF-8 exhibits obviously decreased trend when exposed to 980 nm laser (0.5 W/cm^2), suggesting the efficient generation of ROS from UCNPs-g-C_3N_4−CDs@ ZIF-8. Notably, the ROS production ability is not much different from that in the presence of g-C_3N_4−CDs but markedly higher than that of pure g-C_3N_4. Encouraged by the ROS generation ability of as-prepared composite, which may give rise to effective PDT effect, we used UCNPs-g-C_3N_4−CDs@ZIF-8 composite to evaluate intracellular photodynamic effect by selecting 2′,7′-dichlorofluorescin diacetate (DCFH-DA) dye instead of DPBF to serve as ROS-index probe. DCFH can be oxidized to DCF, which presents bright green fluorescence (λ_{ex} = 488 nm and λ_{em} = 525 nm) in the presence of ROS, which differs from photodegradation reaction of DPBF. In Figure 3C, human cervical carcinoma cell line (HeLa cells) incubated with g-C_3N_4−CDs and UCNPs-g-C_3N_4−CDs@ZIF-8 exposed under 980 nm irradiation demonstrates strong green fluorescence, while the HeLa cells incubated with phosphate-buffered saline (PBS) barely exhibit fluorescence, illustrating that UCNPs-g-C_3N_4−CDs@ZIF-8 composite has good intracellular photodynamic effect.

As known, nontoxicity or low toxicity to body is the basic design principle of ideal therapeutic platform. We first detected the toxicity of pure ZIF-8 using standard 3-(4,5-dimethylthiazol-2-yl)-2,5-diphenyl tetrazolium bromide (MTT) assay. As shown in Figure S7, pure ZIF-8 exhibits low toxicity. Afterward, the cell viability of UCNPs-g-C_3N_4−CDs@ZIF-8 composite for L929 cells was examined (Figure 4A). Encouragingly, after L929 cells are fed with different diluted concentrations of the tested material for 12 and 24 h, the data of cell viability are barely different from that in the control group, indicating any dark cytotoxicity on the viability of cells can be detected even up to a high dose of 500 μg/mL. The data of cell viability in the test group are average calculated by three parallel groups. Besides, we can hardly observe any morphology change and cell apoptosis of L929 cells after cultivated for 12 and 24 h. The results state that UCNPs-g-C_3N_4−CDs@ZIF-8 composite possesses good biocompatibility and non-cytotoxicity to L929 cells. In this work, we did the hemolytic test of UCNPs-g-C_3N_4−CDs@ZIF-8 composite, because the blood hemolysis is another critical factor to the practical biological application. UV−vis spectro-photometer was employed to monitor the absorbance values at 540 nm of suspension solutions obtained by centrifuging the mixture of hemoglobin and various concentrations UCNPs-g-C_3N_4−CDs@ZIF-8 composites. The hemolytic data and the matching digital photographs of the tested materials are displayed in Figure 4B. In this test, the group mixed red blood cells (RBCs) with PBS served as negative control, and pure H_2O served as positive control. Then hemolytic percentage is calculated by hemolytic efficiency $= \frac{A_{\text{sample}} - A_{\text{negative control}}}{A_{\text{positive control}} - A_{\text{negative control}}} \times 100$, and all the highest hemolytic percentages of the tested samples are markedly less than the application value (5%) even up to the highest concentration of 0.5 mg/mL. It shows insignificant hemolysis and no damage to RBCs, which is also proved by the visual inspection of the matching digital photographs.

Moreover, for biomedical application, the stability of UCNPs-g-C_3N_4−CDs@ZIF-8 in physiological environment (such as normal saline, PBS, and cell culture medium) is important. We provided the corresponding data such as the dynamic light scattering (DLS), the surface potential, and absorbance spectra of the UCNPs-g-C_3N_4−CDs@ZIF-8 solutions shocked softly in normal saline and cell medium, PBS for different times of 0, 1, 2, 3, and 5 d at 37 °C to detect the stability. As presented in Figures S8 and S9, the UCNPs-g-C_3N_4−CDs@ZIF-8 nanoparticles were observed with negligible agglomeration after 5 d of incubation, showing remarkable stability in normal saline, PBS, and cell-culture medium (Figure S8A−C). The absorbance intensity and Zeta potentials of UCNPs-g-C_3N_4−CDs@ZIF-8 nanoparticles have a little change

DOI: 10.1021/acsami.6b15203
ACS Appl. Mater. Interfaces 2017, 9, 6829−6838

(Figure S8D). Meanwhile, the DLS properties of UCNPs-*g*-C_3N_4−CDs@ZIF-8 nanoparticles in normal saline, PBS, and cell culture medium were further monitored over a span of 5 d (Figure S9). This study further confirmed the stability of UCNPs-*g*-C_3N_4−CDs@ZIF-8 nanoparticles, as their sizes have no significant change.

From the UC emission spectra and insets in Figure S5, we can see that the UCNPs-*g*-C_3N_4−CDs@ZIF-8 particles are well-dispersed in water and also present strong UC emission under excitation of 980 nm laser. Accordingly, we made experiments to make sure whether UCNPs-*g*-C_3N_4−CDs@ZIF-8 composite could be served as an efficient luminescence probe for bioimaging, and the results are shown in Figure 5.

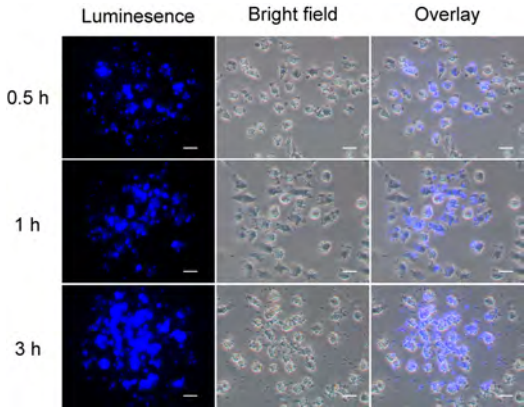

Figure 5. In vitro UCL imaging properties. Inverted fluorescence microscope images of HeLa cells incubated with UCNPs-*g*-C_3N_4−CDs@ZIF-8 for 0.5, 1, and 3 h at 37 °C. Scale bars for all images are 25 μm.

The evidently intracellular up-conversion luminescence (UCL) signals are found, and stronger fluorescence signal is observed, when the incubation time is increased from 0.5 to 3 h, which also suggests the efficient cellular uptake of UCNPs-*g*-C_3N_4−CDs@ZIF-8 composites.

The MTT assay and dye test stained by calcein acetoxymethyl ester (AM)/propidium iodide (PI) were measured for examining the cytotoxicity of UCNPs-*g*-C_3N_4−CDs@ZIF-8 composites in vitro to HeLa cells. The MTT results show (Figure 6A) that no significant difference is observed in the group treated with either laser only or UCNPs-*g*-C_3N_4−CDs@ZIF-8 composite compared with control group, and a high cell viability of more than 80% even up to the high concentration of 1 mg/mL indicates that UCNPs-*g*-C_3N_4−CDs@ZIF-8 particles within wide concentration range induce low cytotoxicity to HeLa cells. The results bring into correspondence with the behavior of biocompatibility test, which is particularly essential for its further biological application. However, the different degrees of downward trend on the cell viability appear when the cells are incubated with UCNPs-*g*-C_3N_4 and UCNPs-*g*-C_3N_4−CDs@ZIF-8 composites (7.8−1000 μg/mL) after irradiation for 5 min at a power density of 0.5 W/cm^2. As expected, the group cultivated with UCNPs-*g*-C_3N_4−CDs@ZIF-8 particles exposed 980 nm laser irradiation shows the strongest inhibitory effect on cancer cells. Compared with the cell viability of the group cultivated with UCNPs-*g*-C_3N_4 composites in the presence of 980 nm laser, it further confirms that dual-modal photodynamic synergistic therapy, implying UCNPs-*g*-C_3N_4−CDs@ZIF-8

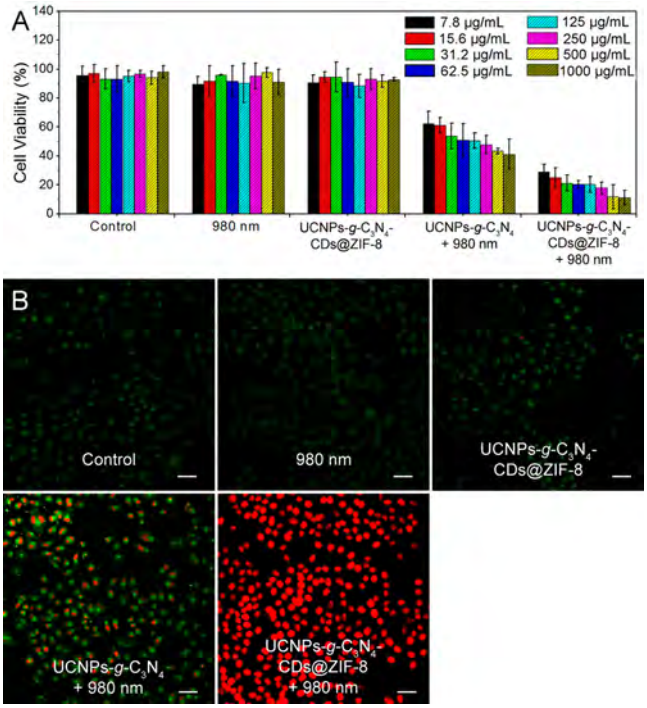

Figure 6. (A) In vitro cell viabilities of HeLa cells incubated with cell-culture (control), 980 nm light, UCNPs-*g*-C_3N_4 with 980 nm laser irradiation, and UCNPs-*g*-C_3N_4−CDs@ZIF-8 at varied concentrations with and without 980 nm laser irradiation. (B) CLSM images of HeLa cells incubated with different conditions corresponding to the toxcity test in vitro, and all the cells are marked with calcein AM and PI. Scale bars for all images are 50 μm.

composite is a more efficient therapeutic project. Similar behaviors are further proved by the confocal laser scanning microscopy (CLSM) images of HeLa cells in the dye experiment. The inhibitory effect on HeLa cells stained with calcein AM and PI is presented in Figure 6B.

The serum biochemistry assay and complete blood count assessment further reveal any potential toxicity of UCNPs-*g*-C_3N_4−CDs@ZIF-8 composite during the treating time. Complete blood counts, blood levels of white blood cells (WBC), red blood cells (RBCs), hematocrit (HCT), hemoglobin (HGB), mean corpuscular volume (MCV), mean corpuscular hemoglobin concentration (MCHC), mean corpuscular hemoglobin (MCH), blood urea level (BUN), alanine aminotransferase (ALT), aspartate aminotransferase (AST), the ratio of albumin and globulin (A/G) and alkaline phosphatase (ALP), and platelets (PLT) of normal saline and UCNPs-*g*-C_3N_4−CDs@ZIF-8 composite treated mice are recorded, and statistic is based on five mice per data point (Table S1). Compared with the control group, all the biochemistry results in the treatment group indicate no clear signal of injury in liver or kidney and no obvious interference with the physiological regulation of immune response for UCNPs-*g*-C_3N_4−CDs@ZIF-8 particles.

The worthy dual-modal photodynamic synergistic therapy in vitro and all the biocompatibility evaluation of UCNPs-*g*-C_3N_4−CDs@ZIF-8 composite encourage us to explore their effectiveness in vivo synergistic therapy against U14 tumor-bearing mouse. Both the body weight change and tumor size increases in the healing process are the major factors to evaluate the toxicity of the tested materials to the living body, so the mice tumor sizes and body weights were monitored 1 d apart,

DOI: 10.1021/acsami.6b15203
ACS Appl. Mater. Interfaces 2017, 9, 6829−6838

and the results are showed in Figure 7. We are thrilled that the body weights increase in all the groups with a steady and

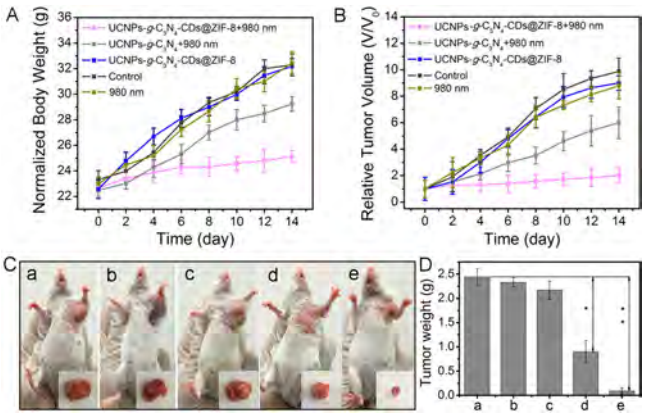

Figure 7. In vivo anticancer properties. (A) The body weight and (B) relative tumor volume of tumor-bearing mice in different groups vs the treatment time. (C) Representative photographs of tumor-bearing mice and tumor tissue excised from tumor-bearing mice treated with (a) normal saline, (b) pure UCNPs-g-C_3N_4−CDs@ZIF-8 composite, (c) 980 nm, (d) pure UCNPs-g-C_3N_4 with 980 nm laser irradiation, and (e) UCNPs-g-C_3N_4−CDs@ZIF-8 with 980 nm laser irradiation on day 14. (D) The weight of tumor excised from tumor-bearing mice. $^*p < 0.01$ vs control group, $^{**}p < 0.01$ vs control group. The data in the figures are average calculated by five mice each group.

sustainable pace in this assay (Figure 7A), and the survival rates of all groups are 100% in the entire treatment process. It suggested that the test material has no acute toxicity to the body. In Figure 7B, the growth rate of tumor exhibits a slight inhibition through cultivating with UCNPs-g-C_3N_4−CDs@ZIF-8 composite without laser irradiation or directly exposing to the laser alone. By contrast, the group treated with UCNPs-g-C_3N_4 composite and exposed to the laser shows the partially delayed tumor tissue and a smallest tumor volume. For mice injected with UCNPs-g-C_3N_4−CDs@ZIF-8 particles and exposed to laser light irradiation, the tumor growth is obviously delayed. This behavior is consistent with the result of ROS assessment in vitro using DCFH-DA as probe. The tumors tissues and the corresponding representative organs are dissected from mouse bearing U14 tumor after treatment for 14 d. Meanwhile, the digital photographs of representative mice and the homologous tumor tissues are showed in Figure 7C. Additionally, the apoptosis and morphology of major organs slices excised from all the treatment groups are monitored by hematoxylin and eosin (H&E) after staining (Figure 8). H&E stained images of organs further demonstrate that our therapeutic reagent has barely acute toxcity to mice.

CONCLUSIONS

In summary, we prepared an excellent dual-photodynamic UCNPs-g-C_3N_4−CDs@ZIF-8 system to achieve enhanced antiproliferation efficacy under hypoxic condition, which combined traits of maximized energy utilization, nontoxicity, and excellent biological compatibility. The resulting system is believed to be able to efficiently transport deeply penetrating photon energy to successively activate the photosensitizers of g-C_3N_4 and CDs, producing ROS rapidly and killing efficiently cancer cells even in the case of hypoxia, according to all the test results. Furthermore, the advent of ZIF-8 shells not only store plenty of O_2 or H_2O needed for photodynamic effect but

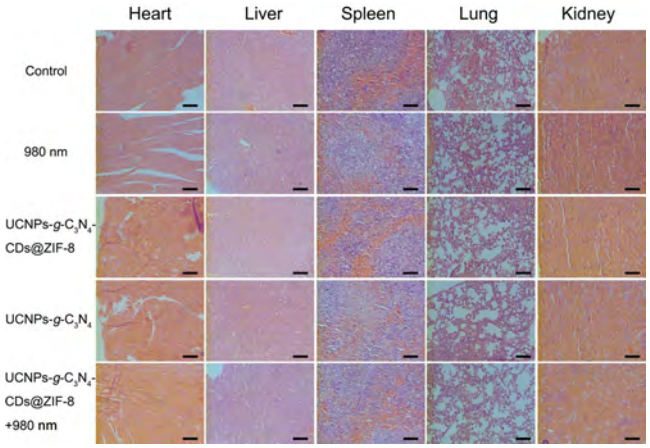

Figure 8. Representative H&E stained histological images of the superficial regions of heart, liver, spleen, lung, and kidney slices. Scale bars for all images are 50 μm.

prevent the fluorescence intensity from being influenced by environment, which is superior to mesoporous silica. The composite is highly efficacious for antiproliferation of cancer cells both in vitro and in vivo. The design of dual-photodynamic treatment system provides an avenue for developing drug carriers with enhanced PDT efficiency, which is clinically applicable in cancer theranostics.

EXPERIMENTAL SECTION

Reagents and Materials. All chemicals and reagents were used as received in this experiment without any further purification, containing Gd_2O_3, Yb_2O_3, and Tm_2O_3 (99.99%) (from Sinopharm Chemical Reagent Co., Ltd., Shanghai, China), nitric acid (HNO_3), ammonium hydroxide ($NH_3{\cdot}H_2O$, 28%), melamine ($C_3H_4N_6$, 99%), cyclohexane, OA, 1-octadecene (ODE), and methanol (from Tianjin Kermel Chemical Reagent Co., Ltd.), PEI (25 kDa), citric acid, zinc nitrate hexahydrate ($Zn(NO_3)_2{\cdot}6H_2O$), 2-methylimidazole (2-MeIm), PBS, ammonium fluoride (NH_4F), sodium hydroxide (NaOH), DPBF, MTT, DMSO, 4′,6-diamidino-2-phenylindole (DAPI), calcein AM, and PI (from Sigma-Aldrich).

Synthesis of g-C_3N_4. The g-C_3N_4 nanosheets were synthesized by calcination process in air integrated with a subsequent liquid exfoliation. Briefly, melamine (5 g) was placed in the semiclosed furnace of 600 °C for 2 h in air with a heating and cooling ramp rate of 3 °C/min, and the bulk g-C_3N_4 yellow powder was obtained. Subsequently, bulk g-C_3N_4 yellow powder (40 mg) was dispersed in deionized water (40 mL) with ultrasonication for ∼14 h. The light-yellow suspension was first centrifuged at 3000 rpm to eliminate the unexfoliated bulk g-C_3N_4, and then the lightly milky suspension was centrifuged at 8000 rpm to retain precipitate for further drying.

Synthesis of CDs. Typically, citric acid (1.0507 g) was dissolved in ultrapure water (30 mL) with stirring until clarification. After ammonium hydroxide (28 wt %) was added, the mixture was transferred to high-pressure reaction vessel heating at 200 °C for 12 h. Then, the yellow solution was dialyzed by dialysis tubing with 3.5 kDa (whose molecular weight cut off (MWCO) was 3500) for 3 d to remove small molecules. The amount of ammonium hydroxide ultimately results in the number of amino on the surface of CDs.[69]

Synthesis of OA-Coated $NaGdF_4$:Yb,Tm@$NaGdF_4$. The OA-coated $NaGdF_4$:Yb, Tm@$NaGdF_4$ nanoparticles were prepared via methanol route with a slight modification.[70] Monodispersed $NaGdF_4$:Yb, Tm were first obtained according to the following process: 1.5 mmol of $RECl_3$ (RE = 75% Gd + 25% Yb + 0.5% Tm) was injected in a 100 mL flask containing OA (6 mL) and ODE (23 mL) and then gradually heated to 90 °C under a vacuum until free of bubbles to remove water content and oxygen. After that, the mixture was heated to 156 °C for 30 min under N_2 protection, to yield light-

DOI: 10.1021/acsami.6b15203
ACS Appl. Mater. Interfaces 2017, 9, 6829−6838

yellow uniform solution, and cooled to 50 °C. Then, methanol solution (15 mL) containing NaOH (3.75 mmol) and NH_4F (6 mmol) were added, and the solution was vigorously stirred more than 30 min. Subsequently, the solution was slowly heated to 90 °C under a vacuum again to remove the impurities with low boiling point and residual water. After the solution was free of bubbles, the temperature was increased to 245 °C, kept there for 45 min in N_2 atmosphere environment, and cooled to room temperature naturally. The $NaGdF_4$:Yb, Tm nanoparticles were collected by centrifugation and alternately washed with ethanol and cyclohexane. Finally, the nanoparticles were dispersed in cyclohexane (5 mL) for later use. For the core−shell synthesis, 1.0 mmol of $GdCl_3$ was injected in a 100 mL flask containing OA (6 mL) and ODE (23 mL), and it was subsequently heated at 110 °C under a vacuum until free of bubbles. After it was flushed with N_2, the solution was heated to 156 °C for 30 min to form homogeneous and transparent solution before cooling to 50 °C. A methanol solution (15 mL) containing NaOH (9 mmol) and NH_4F (5.625 mmol) was slowly added along with the previous core nanoparticels in cyclohexane and vigorously stirred more than 30 min, followed by gradually increasing temperature to 110 °C under a vacuum. After the temperature was increased to 245 °C and kept for 45 min in a N_2 atmosphere, the deep-yellow solution was cooled to room tempreature. The resulting nanoparticles were collected, washed with ethanol and cyclohexane, and redispersed in cyclohexane (5 mL). The core−shell UC nanoparticles $NaGdF_4$:Yb,Tm@$NaGdF_4$ were denoted as UCNPs.

Synthesis of UCNPs-PEI. Typically, a ligand exchange approach was adopted to obtain amino-functionalized UCNPs-PEI using PEI. UCNPs (1.5 mmol) in cyclohexane were injected into PEI aqueous solution (20 mL) containing 2.0 g of PEI, followed by vigorous stirring for 24 h. The obtained product was centrifuged and washed with deionized water to remove unreacted PEI.

Synthesis of UCNPs-*g*-C_3N_4. In brief, the exfoliated *g*-C_3N_4 nanosheets (5 mg) were first dissolved in deionized water. Subsequently, as-prepared UCNPs-PEI nanoparticles were added into *g*-C_3N_4 aqueous solution followed by 4 h of agitation. The resulting UCNPs-*g*-C_3N_4 were collected by centrifugation and washed with deionized water.

Synthesis of UCNPs-*g*-C_3N_4−CDs@ZIF-8. In a typical process, a methanol solution of 2-MeIm (350 mg, 7.2 mL) was first mixed with the aforementioned aqueous solution of UCNPs-*g*-C_3N_4 nanocomposites (2.5 mL) and CDs by sonication, and vigorously stirred at room temperature. Then the methanol solution of $Zn(NO_3)_2$ (150 mg, 7.2 mL) was gradually injected into the above solution over 20 min using a syringe pump to produce UCNPs-*g*-C_3N_4@ZIF-8 particles. Following the addition of $Zn(NO_3)_2$, the reaction solution became milky gradually, showing the formation of ZIF-8 shells. The resulting sample was separated by centrifugation and washed with methanol twice.

ROS Detection. DPBF has been appointed ROS probe in this test, because oxidation and reduction reaction proceed between DPBF with ROS to cause the absorbance, and fluorescence intensities of DPBF, therefore, decreased at 410 nm when the mixture was laser-induced. Operation details are as follows: 10 mg of *g*-C_3N_4, *g*-C_3N_4−CDs, or UCNPs-*g*-C_3N_4−CDs@ZIF-8 composites were added into 2 mL of DPBF stock solution (0.5 mg/mL), respectively, and kept in dark. After ultrasonic treatment, both *g*-C_3N_4 and *g*-C_3N_4−CDs mixed solutions were exposed to 360 nm laser, or then UCNPs-*g*-C_3N_4−CDs@ZIF-8 composites were exposed to 980 nm laser for specific time intervals (5, 10, 15, and 20 min) with the injected atmosphere with low concentration of O_2 to mimic the anaerobic environment, respectively. Finally, a UV−vis spectro-photometer was used to monitor the absorbance of supernatant at 410 nm after centrifuging.

NIR Laser-Induced in Vitro PDT Performance of Composites. The NIR laser-induced in vitro PDT performance to HeLa cells was investigated by using CLSM. In brief, HeLa cells (~5 × 10^4 $well^{-1}$) were cultured in 5% CO_2 at 37 °C for overnight to form a monolayer when it is placed into 6-well culture plates with glass slide. Next, 2 mL/well of the tested materials (1 mg/mL) were injected, and 980 nm laser (0.5 W/cm^2) was used to intermittent optical radiation in the course of cell culture with an atmosphere of 5% O_2 and 5% CO_2 at 37 °C for another 4 h to mimic the anaerobic environment. After residual material was removed thoroughly by washing three times with PBS, the cells were stained with DCFH-DA for 20 min. Finally, the results were monitored by CLSM.

In Vitro Cell Viability of UCNPs-*g*-C_3N_4−CDs@ZIF-8 Composites. Appraising the toxicity of UCNPs-*g*-C_3N_4−CDs@ZIF-8 composites to L929 fibroblast cells usually call MTT assay to help. First, L929 fibroblast cells at a density of ~7500 per well were placed into a 96-well plate. After the cell line grew with adherence and formed a monolayer at simulated normal body temperature condition (5% CO_2, 37 °C), 0.1 mL of UCNPs-*g*-C_3N_4−CDs@ZIF-8 composites with diluted concentration (7.8, 15.6, 31.3, 62.5, 125, 250, and 500 μg/mL) was injected into each well. For the material to get to cells, the mixture was placed for another 12 or 24 h. Next, 0.02 mL/well of the as-prepared MTT stock solution (5 mg/mL) was mixed and sequentially cultured for 4 h (5% CO_2, 37 °C). Prior to 0.15 mL/well of DMSO was added, thoroughly remove the suspension. Many results demonstrated: The metabolism of living cells can reduce MTT to produce water-insoluble formazan using cytochrome c, and the absorbance at 488 nm of formazan is directly proportional to the amount of living cells. So, the 96-well plate plate was shocked for 5 min for the formazan to completely dissolve in DMSO solvent, and then it was measured using a microplate reader. Meanwhile, a confocal laser scanning microscope (Leica TCS SP8) was employed to detect the morphology of L929 cells for 12 and 24 h. The data in this test are average calculated by the three paralleled groups of each concentration.

Hemolysis Assay. To get RBCs, we washed the EDTA.K2 stabilized human blood with PBS and centrifuged until the supernatant solution become transparent. Then, the obtained RBCs were diluted by PBS with the volume proportion of 1:10. Diluted RBCs (0.3 mL) suspension placed within tube is being mixed with 1.2 mL of PBS, deionized water, and UCNPs-*g*-C_3N_4−CDs@ZIF-8 (15.6, 31.3, 62.5, 125, 250, and 500 μg/mL) to detect the absorbance at 541 nm of the upper supernatants using UV−vis spectroscopy after shake the tube and rest for 2 h.

In Vitro Cytotoxicity of UCNPs-*g*-C_3N_4−CDs@ZIF-8 Composites. The detection process of biocompatibility to L929 fibroblast cells in vitro also can be applied to cytotoxicity test to cancer cells in vitro. Instead of L929 fibroblast cells, HeLa cancer cells were cultivated in a cell medium with an atmosphere of 5% O_2 and 5% CO_2 at 37 °C to mimic the anaerobic environment and various certain concentrations of pure UCNPs-*g*-C_3N_4−CDs@ZIF-8 composites, UCNPs-*g*-C_3N_4 composites with 980 nm laser irradiation, and UCNPs-*g*-C_3N_4−CDs@ZIF-8 composites with 980 nm laser irradiation in the MTT assay. Besides, the group treated with PBS was employed as control blank group.

The detection process of dye experiment in vitro has a strong resemblance to that of photodynamic effects, except that the live and dead cells were stained with calcein AM (2 mM) and PI (5 mM) for 1 h.

Up-Conversion Luminescence Microscopy Observation of UCNPs-*g*-C_3N_4−CDs@ZIF-8 Composite. In brief, HeLa cells (~5 × 10^4 $well^{-1}$) were cultured overnight and formed a monolayer when it is placed into 6-well culture plates with glass slide. Then, 2 mL of as-prepared UCNPs-*g*-C_3N_4−CDs@ZIF-8 (0.5 mg/mL) was injected for specific cultivating time (0.5, 1, and 3 h, respectively) at simulated normal body temperature, rinsing the cells three times with PBS at the indicated time points after removal of the culture medium. Subsequently, 1 mL/well formaldehyde (2.5%) was fixed with the cells at 37 °C for 10 min and rinsed three times with PBS again. Finally, all collected cells were monitored by UC luminescence microscopy.

Animal Experiments and ex Vivo Histological Staining. Each female Balb/c mice (25−30 g) injected U14 cells (murine cervical carcinoma cell lines) into the left subaxilla were partitioned into five evenly distributed groups. The tumor-bearing mice with bean-size tumorlike feature were cultured with different test condition, including normal saline, pure 980 nm laser irradiation, pure UCNPs-*g*-C_3N_4−

DOI: 10.1021/acsami.6b15203
ACS Appl. Mater. Interfaces 2017, 9, 6829−6838

CDs@ZIF-8 composites, UCNPs-g-C_3N_4 composites with 980 nm laser irradiation, and UCNPs-g-C_3N_4−CDs@ZIF-8 composites with 980 nm laser irradiation. Just as we know, the group treated with normal saline as control black group, and the tumor site exposed to 980 nm laser (0.5 W/cm^2) for 10 min after intravenous injection of the different materials for 12 h. In vivo biodistribution result in Figure S10 verifies that 12 h postinjection is the optimal time point. In this work, each mouse was injected with 0.1 mL of tested materials (1 mg/mL) 1 d apart, and the tumor volumes and body weights of each mouse were interval recorded every other day, meanwhile. After 14 d of treatment, the tumor-bearing mice were sacrificed to collect the blood, for blood biochemistry and hematology analysis, and to dissect the tumor tissues and typical organs (heart, liver, spleen, lung, and kidney) for further histology analysis.

Characterization. XRD measurements were performed on a Rigaku D/max-TTR-III diffractometer using Cu Kα radiation (λ = 0.154 05 nm). SEM micrographs were measured on a scanning electron microscope (SEM, JSM-6480A, Japan Electronics). TEM images were recorded on an FEI Tecnai G^2 S-Twin with a field emission gun operating at 200 kV. N_2 absorption/desorption isotherms were obtained at 77 K using a Micromeritics ASAP TriStar II instrument. The specific surface area was determined through the Brunauer−Emmett−Teller method. The pore size distribution was calculated by the Barret−Joner−Halenda method. Atomic force microscope (AFM) images were recorded by CSPM5500. The X-ray photoelectron spectrum (XPS) was measured on a VG ESCALAB MK II electron energy spectrometer using Mg KR (1253.6 eV) as the X-ray excitation source. FT-IR spectra were obtained on a PerkinElmer 580B IR spectro-photometer using the KBr pellet as the background. UCL emission spectra were obtained using 980 nm LD Module (K98D08M-30W, China) as the excitation source and detected by R955 (Hamamatsu) from 400 to 900 nm. All the UC spectra in our experiment were gained under the same condition with the same signal amplification. UV−vis spectra were detected by UV-1601 spectro-photometer. CLSM images were recorded using Leica SP8. The UCL images were obtained on Nikon Ti−S with an external 980 nm laser irradiation.

■ ASSOCIATED CONTENT

Supporting Information

The Supporting Information is available free of charge on the ACS Publications website at DOI: 10.1021/acsami.6b15203.

FT-IR spectra of OA-UCNPs and PEI-UCNPs; TEM images of g-C_3N_4 sheets, AFM image of g-C_3N_4 sheets and their height profiles; XRD patterns of as-prepared samples; N_2 adsorption/desorption isotherm of UCNPs-g-C_3N_4−CDs@ZIF-8; emission spectra of NaGdF$_4$:Yb,Tm, NaGdF$_4$:Yb,Tm@NaGdF$_4$, UCNPs-g-C_3N_4−CDs@ZIF-8 and their corresponding photographs under 980 nm laser excitation; time-course absorbance spectrum of DPBF mixed with UCNPs-g-C_3N_4−CDs@ZIF-8 at the wavelength of 410 nm under 980 nm laser (0.5 W/cm^2); cell toxicity of pure ZIF-8 nanoparticles; photographs and absorbance spectra of the UCNPs-g-C_3N_4−CDs@ZIF-8 solutions in PBS, normal saline and cell medium (10% fetal bovine serum) after 5 d of standing, Zeta potentials of as-made UCNPs-g-C_3N_4−CDs@ZIF-8 in PBS, normal saline and cell medium (10% fetal bovine serum) after 5 d of standing; DLS size distribution of UCNPs-g-C_3N_4−CDs@ZIF-8 in PBS, normal saline and cell medium with 10% fetal bovine serum after 5 d of standing; the biodistribution of Gd in major organs and tumor of mice after injection of UCNPs-g-C_3N_4−CDs@ZIF-8 nanoparticles intravenously at different time points; blood biochemistry and hematology data of female Balb/c mice at 14 d (PDF)

■ AUTHOR INFORMATION

Corresponding Authors

*E-mail: gaishili@hrbeu.edu.cn. (S.G.)

*E-mail: yangpiaoping@hrbeu.edu.cn. (P.Y.)

ORCID

Piaoping Yang: 0000-0002-9555-1803

Author Contributions

The manuscript was written through contributions of all authors. All authors have given approval to the final version of the manuscript.

Notes

The authors declare no competing financial interest.

■ ACKNOWLEDGMENTS

Financial support from the National Natural Science Foundation of China (NSFC 21401032, 51472058, 51502050, 51422209, and 51572258), China Postdoctoral Science Foundation (2014M560248 and 2015T80321), Natural Science Foundation of Heilongjiang Province (B201403), Outstanding Youth Foundation of Heilongjiang Province (JC2015003), Heilongjiang Postdoctoral Fund (LBH-Z14052 and LBH-TZ0607), and the Fundamental Research funds for the Central Universities are greatly acknowledged.

■ REFERENCES

(1) Idris, N. M.; Gnanasammandhan, M. K.; Zhang, J.; Ho, P. C.; Mahendran, R.; Zhang, Y. *In Vivo* Photodynamic Therapy Using Upconversion Nanoparticles as Remote-Controlled Nanotransducers. *Nat. Med.* **2012**, *18*, 1580−U190.

(2) Wang, F.; Chen, X. L.; Zhao, Z. X.; Tang, S. H.; Huang, X. Q.; Lin, C. H.; Cai, C. B.; Zheng, N. F. Synthesis of Magnetic, Fluorescent And Mesoporous Core-Shell-Structured Nanoparticles for Imaging, Targeting and Photodynamic Therapy. *J. Mater. Chem.* **2011**, *21*, 11244−11252.

(3) Yuan, J.; Cen, Y.; Kong, X. J.; Wu, S.; Liu, C. L. W.; Yu, R. Q.; Chu, X. MnO_2-Nanosheet-Modified Upconversion Nanosystem for Sensitive Turn-On Fluorescence Detection of H_2O_2 and Glucose in Blood. *ACS Appl. Mater. Interfaces* **2015**, *7*, 10548−10555.

(4) Gai, S.; Li, C.; Yang, P.; Lin, J. Recent Progress in Rare Earth Micro/Nanocrystals: Soft Chemical Synthesis, Luminescent Properties, and Biomedical Applications. *Chem. Rev.* **2014**, *114*, 2343−2389.

(5) Hu, Y.; Yang, Y. M.; Wang, H. J.; Du, H. Synergistic Integration of Layer-by-Layer Assembly of Photosensitizer and Gold Nanorings for Enhanced Photodynamic Therapy in the Near Infrared. *ACS Nano* **2015**, *9*, 8744−8754.

(6) Chen, R.; Zhang, J. F.; Wang, Y.; Chen, X. F.; Zapien, J. A.; Lee, C. S. Graphitic Carbon Nitride Nanosheet@Metal-Organic Framework Core-Shell Nanoparticles for Photo-Chemo Combination Therapy. *Nanoscale* **2015**, *7*, 17299−17305.

(7) Huang, P.; Lin, J.; Wang, X. S.; Wang, Z.; Zhang, C. L.; He, M.; Wang, K.; Chen, F.; Li, Z. M.; Shen, G. X.; Cui, D. X.; Chen, X. Y. Light-Triggered Theranostics Based on Photosensitizer-Conjugated Carbon Dots for Simultaneous Enhanced-Fluorescence Imaging and Photodynamic Therapy. *Adv. Mater.* **2012**, *24*, 5104−5110.

(8) Idris, N. M.; Lucky, S. S.; Li, Z. Q.; Huang, K.; Zhang, Y. Photoactivation of Core-Shell Titania Coated Upconversion Nanoparticles and Their Effect on Cell Death. *J. Mater. Chem. B* **2014**, *2*, 7017−7026.

(9) Lu, S.; Tu, D. T.; Hu, P.; Xu, J.; Li, R. F.; Wang, M.; Chen, Z.; Huang, M. D.; Chen, X. Y. Multifunctional Nano-Bioprobes Based on Rattle-Structured Upconverting Luminescent Nanoparticles. *Angew. Chem., Int. Ed.* **2015**, *54*, 7915−7919.

(10) Pan, L. M.; Liu, J. A.; Shi, J. L. Intranuclear Photosensitizer Delivery and Photosensitization for Enhanced Photodynamic Therapy with Ultralow Irradiance. *Adv. Funct. Mater.* **2014**, *24*, 7318−7327.

DOI: 10.1021/acsami.6b15203
ACS Appl. Mater. Interfaces 2017, 9, 6829−6838

(11) Liu, X. M.; Que, I.; Kong, X. G.; Zhang, Y. L.; Tu, L. P.; Chang, Y. L.; Wang, T. T.; Chan, A.; Lowik, C.; Zhang, H. *In Vivo* 808 nm Image-Guided Photodynamic Therapy Based on an Upconversion Theranostic Nanoplatform. *Nanoscale* **2015**, *7*, 14914−14923.
(12) Hou, Z.; Zhang, Y.; Deng, K.; Chen, Y.; Li, X.; Deng, X.; Cheng, Z.; Lian, H.; Li, C.; Lin, J. UV-Emitting Upconversion-Based TiO_2 Photosensitizing Nanoplatform: Near-Infrared Light Mediated *in Vivo* Photodynamic Therapy *via* Mitochondria-Involved Apoptosis Pathway. *ACS Nano* **2015**, *9*, 2584−2599.
(13) Turan, I. S.; Yildiz, D.; Turksoy, A.; Gunaydin, G.; Akkaya, E. U. A Bifunctional Photosensitizer for Enhanced Fractional Photodynamic Therapy: Singlet Oxygen Generation in the Presence and Absence of Light. *Angew. Chem., Int. Ed.* **2016**, *55*, 2875−2878.
(14) Yue, X. L.; Yanez, C. O.; Yao, S.; Belfield, K. D. Selective Cell Death by Photochemically Induced pH Imbalance in Cancer Cells. *J. Am. Chem. Soc.* **2013**, *135*, 2112−2115.
(15) Jin, C. S.; Lovell, J. F.; Chen, J.; Zheng, G. Ablation of Hypoxic Tumors with Dose-Equivalent Photothermal, but Not Photodynamic, Therapy Using a Nanostructured Porphyrin Assembly. *ACS Nano* **2013**, *7*, 2541−2550.
(16) Heinrich, T. A.; Tedesco, A. C.; Fukuto, J. M.; da Silva, R. S. Production of Reactive Oxygen and Nitrogen Species by Light Irradiation of a Nitrosyl Phthalocyanine Ruthenium Complex as a Strategy for Cancer Treatment. *Dalton Trans.* **2014**, *43*, 4021−4025.
(17) Erler, J. T.; Bennewith, K. L.; Nicolau, M.; Dornhofer, N.; Kong, C.; Le, Q. T.; Chi, J. T. A.; Jeffrey, S. S.; Giaccia, A. J. Lysyl Oxidase is Essential for Hypoxia-Induced Metastasis. *Nature* **2006**, *440*, 1222−1226.
(18) Zhu, W. W.; Dong, Z. L.; Fu, T. T.; Liu, J. J.; Chen, Q.; Li, Y. G.; Zhu, R.; Xu, L. G.; Liu, Z. Modulation of Hypoxia in Solid Tumor Microenvironment with MnO_2 Nanoparticles to Enhance Photodynamic Therapy. *Adv. Funct. Mater.* **2016**, *26*, 5490−5498.
(19) Liu, Y. Y.; Liu, Y.; Bu, W. B.; Cheng, C.; Zuo, C. J.; Xiao, Q. F.; Sun, Y.; Ni, D. L.; Zhang, C.; Liu, J. A.; Shi, J. L. Hypoxia Induced by Upconversion-Based Photodynamic Therapy: Towards Highly Effective Synergistic Bioreductive Therapy in Tumors. *Angew. Chem., Int. Ed.* **2015**, *54*, 8105−8109.
(20) Hu, D. H.; Sheng, Z. H.; Gao, G. H.; Siu, F. M.; Liu, C. B.; Wan, Q.; Gong, P.; Zheng, H. R.; Ma, Y. F.; Cai, L. T. Activatable Albumin-Photosensitizer Nanoassemblies for Triple-Modal Imaging and Thermal-Modulated Photodynamic Therapy of Cancer. *Biomaterials* **2016**, *93*, 10−19.
(21) Chen, Y.; Tan, C.; Zhang, H.; Wang, L. Two-Dimensional Graphene Analogues for Biomedical Applications. *Chem. Soc. Rev.* **2015**, *44*, 2681−2701.
(22) Brown, S. B.; Brown, E. A.; Walker, I. The Present and Future Role of Photodynamic Therapy in Cancer Treatment. *Lancet Oncol.* **2004**, *5*, 497−508.
(23) Li, Y. Y.; Wen, T.; Zhao, R. F.; Liu, X. X.; Ji, T. J.; Wang, H.; Shi, X. W.; Shi, J.; Wei, J. Y.; Zhao, Y. L.; Wu, X. C.; Nie, G. J. Localized Electric Field of Plasmonic Nanoplatform Enhanced Photodynamic Tumor Therapy. *ACS Nano* **2014**, *8*, 11529−11542.
(24) Zhang, C.; Zhao, K. L.; Bu, W. B.; Ni, D. L.; Liu, Y. Y.; Feng, J. W.; Shi, J. L. Marriage of Scintillator and Semiconductor for Synchronous Radiotherapy and Deep Photodynamic Therapy with Diminished Oxygen Dependence. *Angew. Chem., Int. Ed.* **2015**, *54*, 1770−1774.
(25) Kachynski, A. V.; Pliss, A.; Kuzmin, A. N.; Ohulchanskyy, T. Y.; Baev, A.; Qu, J.; Prasad, P. N. Photodynamic Therapy by *in Situ* Nonlinear Photon Conversion. *Nat. Photonics* **2014**, *8*, 455−461.
(26) Liu, J.; Liu, Y.; Liu, N. Y.; Han, Y. Z.; Zhang, X.; Huang, H.; Lifshitz, Y.; Lee, S. T.; Zhong, J.; Kang, Z. H. Metal-Free Efficient Photocatalyst for Stable Visible Water Splitting *via* a Two-Electron Pathway. *Science* **2015**, *347*, 970−974.
(27) Martin, D. J.; Reardon, P. J. T.; Moniz, S. J. A.; Tang, J. W. Visible Light-Driven Pure Water Splitting by a Nature-Inspired Organic Semiconductor-Based System. *J. Am. Chem. Soc.* **2014**, *136*, 12568−12571.
(28) Chen, C. K.; Chen, H. M.; Chen, C. J.; Liu, R. S. Plasmon-Enhanced Near-Infrared-Active Materials In Photoelectrochemical Water Splitting. *Chem. Commun.* **2013**, *49*, 7917−7919.
(29) Dong, Q. F.; Fang, Y. J.; Shao, Y. C.; Mulligan, P.; Qiu, J.; Cao, L.; Huang, J. S. Electron-Hole Diffusion Lengths > 175 μm in Solution-Grown $CH_3NH_3PbI_3$ Single Crystals. *Science* **2015**, *347*, 967−970.
(30) Cao, S. W.; Low, J. X.; Yu, J. G.; Jaroniec, M. Polymeric Photocatalysts Based on Graphitic Carbon Nitride. *Adv. Mater.* **2015**, *27*, 2150−2176.
(31) Highfield, J. Advances and Recent Trends in Heterogeneous Photo(Electro)-Catalysis for Solar Fuels and Chemicals. *Molecules* **2015**, *20*, 6739−6793.
(32) Yin, S. M.; Han, J. Y.; Zhou, T. H.; Xu, R. Recent Progress in g-C_3N_4 Based Low Cost Photocatalytic System: Activity Enhancement and Emerging Applications. *Catal. Sci. Technol.* **2015**, *5*, 5048−5061.
(33) Bai, X. J.; Yan, S. C.; Wang, J. J.; Wang, L.; Jiang, W. J.; Wu, S. L.; Sun, C. P.; Zhu, Y. F. A Simple And Efficient Strategy for the Synthesis of a Chemically Tailored g-C_3N_4 Material. *J. Mater. Chem. A* **2014**, *2*, 17521−17529.
(34) Lin, L. S.; Cong, Z. X.; Li, J.; Ke, K. M.; Guo, S. S.; Yang, H. H.; Chen, G. N. Graphitic-Phase C_3N_4 Nanosheets as Efficient Photosensitizers and pH-Responsive Drug Nanocarriers for Cancer Imaging And Therapy. *J. Mater. Chem. B* **2014**, *2*, 1031−1037.
(35) Liu, J. H.; Zhang, Y. W.; Lu, L. H.; Wu, G.; Chen, W. Self-Regenerated Solar-Driven Photocatalytic Water-Splitting by Urea Derived Graphitic Carbon Nitride With Platinum Nanoparticles. *Chem. Commun.* **2012**, *48*, 8826−8828.
(36) Chan, C. F.; Zhou, Y.; Guo, H. Y.; Zhang, J. Y.; Jiang, L. J.; Chen, W.; Shiu, K. K.; Wong, W. K.; Wong, K. L. pH-Dependent Cancer-Directed Photodynamic Therapy by a Water-Soluble Graphitic-Phase Carbon Nitride-Porphyrin Nanoprobe. *ChemPlusChem* **2016**, *81*, 535−540.
(37) Wan, H.; Zhang, Y.; Zhang, W. B.; Zou, H. F. Robust Two-Photon Visualized Nanocarrier with Dual Targeting Ability for Controlled Chemo-Photodynamic Synergistic Treatment of Cancer. *ACS Appl. Mater. Interfaces* **2015**, *7*, 9608−9618.
(38) Li, H. T.; Kang, Z. H.; Liu, Y.; Lee, S. T. Carbon Nanodots: Synthesis, Properties and Applications. *J. Mater. Chem.* **2012**, *22*, 24230−24253.
(39) Ming, H.; Ma, Z.; Liu, Y.; Pan, K. M.; Yu, H.; Wang, F.; Kang, Z. H. Large Scale Electrochemical Synthesis of High Quality Carbon Nanodots and Their Photocatalytic Property. *Dalton Trans.* **2012**, *41*, 9526−9531.
(40) He, L.; Wang, T. T.; An, J. P.; Li, X. M.; Zhang, L. Y.; Li, L.; Li, G. Z.; Wu, X. T.; Su, Z. M.; Wang, C. G. Carbon Nanodots@Zeolitic Imidazolate Framework-8 Nanoparticles for Simultaneous Ph-Responsive Drug Delivery and Fluorescence Imaging. *CrystEngComm* **2014**, *16*, 3259−3263.
(41) Li, X. F.; Ren, H.; Zou, Z. J.; Sun, J. J.; Wang, J. Y.; Liu, Z. H. Energy Gap Engineering of Polymeric Carbon Nitride Nanosheets for Matching with $NaYF_4$:Yb,Tm: Enhanced Visible-Near Infrared Photocatalytic Activity. *Chem. Commun.* **2016**, *52*, 453−456.
(42) Xu, X. Y.; Ray, R.; Gu, Y. L.; Ploehn, H. J.; Gearheart, L.; Raker, K.; Scrivens, W. A. Electrophoretic Analysis and Purification of Fluorescent Single-Walled Carbon Nanotube Fragments. *J. Am. Chem. Soc.* **2004**, *126*, 12736−12737.
(43) Ge, J. C.; Jia, Q. Y.; Liu, W. M.; Lan, M. H.; Zhou, B. J.; Guo, L.; Zhou, H. Y.; Zhang, H. Y.; Wang, Y.; Gu, Y.; Meng, X. M.; Wang, P. F. Carbon Dots with Intrinsic Theranostic Properties for Bioimaging, Red-Light-Triggered Photodynamic/Photothermal Simultaneous Therapy *In Vitro* and *In Vivo*. *Adv. Healthcare Mater.* **2016**, *5*, 665−675.
(44) Feng, T.; Ai, X. Z.; Ong, H. M.; Zhao, Y. L. Dual-Responsive Carbon Dots for Tumor Extracellular Microenvironment Triggered Targeting and Enhanced Anticancer Drug Delivery. *ACS Appl. Mater. Interfaces* **2016**, *8*, 18732−18740.
(45) Jia, X.; Pei, M. L.; Zhao, X. B.; Tian, K.; Zhou, T. T.; Liu, P. PEGylated Oxidized Alginate-DOX Prodrug Conjugate Nanoparticles

DOI: 10.1021/acsami.6b15203
ACS Appl. Mater. Interfaces 2017, 9, 6829−6838

Cross-Linked with Fluorescent Carbon Dots for Tumor Theranostics. *ACS Biomater. Sci. Eng.* **2016**, *2*, 1641−1648.
(46) Ge, J.; Lan, M.; Zhou, B.; Liu, W.; Guo, L.; Wang, H.; Jia, Q.; Niu, G.; Huang, X.; Zhou, H.; Meng, X.; Wang, P.; Lee, C.-S.; Zhang, W.; Han, X. A graphene Quantum Dot Photodynamic Therapy Agent with High Singlet Oxygen Generation. *Nat. Commun.* **2014**, *5*, 4596−4605.
(47) Ge, J.; Jia, Q.; Liu, W.; Guo, L.; Liu, Q.; Lan, M.; Zhang, H.; Meng, X.; Wang, P. Red-Emissive Carbon Dots for Fluorescent, Photoacoustic, and Thermal Theranostics in Living Mice. *Adv. Mater.* **2015**, *27*, 4169−4177.
(48) van Veggel, F. Near-Infrared Quantum Dots and Their Delicate Synthesis, Challenging Characterization, and Exciting Potential Applications. *Chem. Mater.* **2014**, *26*, 111−122.
(49) Li, H. T.; Liu, R. H.; Lian, S. Y.; Liu, Y.; Huang, H.; Kang, Z. H. Near-Infrared Light Controlled Photocatalytic Activity of Carbon Quantum Dots for Highly Selective Oxidation Reaction. *Nanoscale* **2013**, *5*, 3289−3297.
(50) Liu, R. H.; Huang, H.; Li, H. T.; Liu, Y.; Zhong, J.; Li, Y. Y.; Zhang, S.; Kang, Z. H. Metal Nanoparticle/Carbon Quantum Dot Composite as a Photocatalyst for High-Efficiency Cyclohexane Oxidation. *ACS Catal.* **2014**, *4*, 328−336.
(51) Huang, X. Y. Realizing Efficient Upconversion and Down-Shifting Dual-Mode Luminescence in Lanthanide-Doped $NaGdF_4$ Core-Shell-Shell Nanoparticles through Gadolinium Sublattice-Mediated Energy Migration. *Dyes Pigm.* **2016**, *130*, 99−105.
(52) Dai, Y. L.; Xiao, H. H.; Liu, J. H.; Yuan, Q. H.; Ma, P. A.; Yang, D. M.; Li, C. X.; Cheng, Z. Y.; Hou, Z. Y.; Yang, P. P.; Lin, J. *In Vivo* Multimodality Imaging and Cancer Therapy by Near-Infrared Light-Triggered trans-Platinum Pro-Drug-Conjugated Upconverison Nanoparticles. *J. Am. Chem. Soc.* **2013**, *135*, 18920−18929.
(53) He, F.; Yang, G. X.; Yang, P. P.; Yu, Y. X.; Lv, R. C.; Li, C. X.; Dai, Y. L.; Gai, S. L.; Lin, J. A New Single 808 nm NIR Light-Induced Imaging-Guided Multifunctional Cancer Therapy Platform. *Adv. Funct. Mater.* **2015**, *25*, 3966−3976.
(54) Ai, X. Z.; Ho, C. J. H.; Aw, J.; Attia, A. B. E.; Mu, J.; Wang, Y.; Wang, X. Y.; Wang, Y.; Liu, X. G.; Chen, H. B.; Gao, M. Y.; Chen, X. Y.; Yeow, E. K. L.; Liu, G.; Olivo, M.; Xing, B. G. *In Vivo* Covalent Cross-Linking of Photon-Converted Rare-Earth Nanostructures for Tumour Localization and Theranostics. *Nat. Commun.* **2016**, *7*, 10432−10442.
(55) Wang, C.; Cheng, L.; Liu, Z. Upconversion Nanoparticles for Photodynamic Therapy and other Cancer Therapeutics. *Theranostics* **2013**, *3*, 317−330.
(56) Wang, C.; Tao, H. Q.; Cheng, L.; Liu, Z. Near-Infrared Light Induced *in Vivo* Photodynamic Therapy of Cancer Based on Upconversion Nanoparticles. *Biomaterials* **2011**, *32*, 6145−6154.
(57) Wang, F.; Banerjee, D.; Liu, Y. S.; Chen, X. Y.; Liu, X. G. Upconversion Nanoparticles in Biological Labeling, Imaging, and Therapy. *Analyst* **2010**, *135*, 1839−1854.
(58) Guan, M.; Dong, H.; Ge, J.; Chen, D.; Sun, L.; Li, S.; Wang, C.; Yan, C.; Wang, P.; Shu, C. Multifunctional Upconversion-Nanoparticles-Trismethylpyridylporphyrin- Fullerene Nanocomposite: a Near-Infrared Light-Triggered Theranostic Platform for Imaging-Guided Photodynamic Therapy. *NPG Asia Mater.* **2015**, *7*, e205.
(59) Yang, D.; Ma, P. a.; Hou, Z.; Cheng, Z.; Li, C.; Lin, J. Current Advances in Lanthanide Ion Ln^{3+}-Based Upconversion Nanomaterials for Drug Delivery. *Chem. Soc. Rev.* **2015**, *44*, 1416−1448.
(60) Zhang, Z.; Chen, Y.; Xu, X.; Zhang, J.; Xiang, G.; He, W.; Wang, X. Well-Defined Metal-Organic Framework Hollow Nanocages. *Angew. Chem., Int. Ed.* **2014**, *53*, 429−433.
(61) Lu, K. D.; He, C. B.; Lin, W. B. A Chlorin-Based Nanoscale Metal-Organic Framework for Photodynamic Therapy of Colon Cancers. *J. Am. Chem. Soc.* **2015**, *137*, 7600−7603.
(62) Guo, H. L.; Zhu, Y. Z.; Wang, S.; Su, S. Q.; Zhou, L.; Zhang, H. J. Combining Coordination Modulation with Acid-Base Adjustment for the Control over Size of Metal-Organic Frameworks. *Chem. Mater.* **2012**, *24*, 444−450.
(63) Corma, A.; Garcia, H.; Llabres i Xamena, F. X. L. I. Engineering Metal Organic Frameworks for Heterogeneous Catalysis. *Chem. Rev.* **2010**, *110*, 4606−4655.
(64) Zheng, X. P.; Shi, J. X.; Bu, Y.; Tian, G.; Zhang, X.; Yin, W. Y.; Gao, B. F.; Yang, Z. Y.; Hu, Z. B.; Liu, X. F.; Yan, L.; Gu, Z. J.; Zhao, Y. L. Silica-Coated Bismuth Sulfide Nanorods as Multimodal Contrast Agents for a Non-Invasive Visualization of the Gastrointestinal Tract. *Nanoscale* **2015**, *7*, 12581−12591.
(65) Zhao, C.; Feng, L. Y.; Xu, B. L.; Ren, J. S.; Qu, X. G. Synthesis and Characterization of Red-Luminescent Graphene Oxide Functionalized with Silica-Coated Eu^{3+} Complex Nanoparticles. *Chem. - Eur. J.* **2011**, *17*, 7007−7012.
(66) Yang, D.; Yang, G. X.; Wang, X. M.; Lv, R. C.; Gai, S. L.; He, F.; Gulzar, A.; Yang, P. P. Y_2O_3:Yb,Er@mSiO_2-Cu_xS Double-Shelled Hollow Spheres for Enhanced Chemo-/Photothermal Anti-Cancer Therapy and Dual-Modal Imaging. *Nanoscale* **2015**, *7*, 12180−12191.
(67) Xiong, L. Q.; Yang, T. S.; Yang, Y.; Xu, C. J.; Li, F. Y. Long-Term *in Vivo* Biodistribution Imaging and Toxicity of Polyacrylic Acid-Coated Upconversion Nanophosphors. *Biomaterials* **2010**, *31*, 7078−7085.
(68) Haase, M.; Schafer, H. Upconverting Nanoparticles. *Angew. Chem., Int. Ed.* **2011**, *50*, 5808−5829.
(69) Wang, S. D.; Zhu, Z. F.; Chang, Y. J.; Wang, H.; Yuan, N.; Li, G. P.; Yu, D. B.; Jiang, Y. Ammonium Hydroxide Modulated Synthesis of High-Quality Fluorescent Carbon Dots for White Leds with Excellent Color Rendering Properties. *Nanotechnology* **2016**, *27*, 295202−295211.
(70) Wang, F.; Han, Y.; Lim, C. S.; Lu, Y. H.; Wang, J.; Xu, J.; Chen, H. Y.; Zhang, C.; Hong, M. H.; Liu, X. G. Simultaneous Phase and Size Control of Upconversion Nanocrystals through Lanthanide Doping. *Nature* **2010**, *463*, 1061−1065.

DOI: 10.1021/acsami.6b15203
ACS Appl. Mater. Interfaces 2017, 9, 6829−6838